Monthly Notices
of the
ROYAL ASTRONOMICAL SOCIETY

MNRAS **459,** 4161–4173 (2016)
Advance Access publication 2016 April 22

doi:10.1093/mnras/stw961

# The apparent synchronization of V1500 Cygni

Thomas E. Harrison[1]★ and Ryan K. Campbell[2]

[1]*Department of Astronomy, New Mexico State University, Box 30001, MSC 4500, Las Cruces, NM 88003-8001, USA*
[2]*Department of Physics and Astronomy, Humboldt State University, 1 Harpst St, Arcata, CA 95521, USA*

Accepted 2016 April 19. Received 2016 April 19; in original form 2016 January 29

**ABSTRACT**

We have used *XMM–Newton* and ground-based optical/near-infrared photometry to explore the old classical nova, and asynchronous polar V1500 Cyg. The X-ray light curve shows a single bright phase once per orbit, associated with the main accretion region. Analysis of the X-ray light curve indicates that the white dwarf spin period is now similar to the orbital period. When this inference is combined with the ground-based photometry, we find that the most probable explanation for the observed behaviour is a system that has become fully synchronized. The X-ray spectrum and luminosity of V1500 Cyg are consistent with a high state polar. The optical and near-IR light curves can partially be explained as a heavily irradiated secondary star, but exhibit strong deviations from that model. We find that the most likely explanation for the observed excesses in these light curves is cyclotron emission from distributed accretion regions, or from a multipole geometry.

**Key words:** stars: individual: V1500 Cygni – infrared: stars – X-rays: stars.

## 1 INTRODUCTION

V1500 Cyg, Nova Cygni 1975, vies with CP Pup for the title of the most luminous classical nova ever observed, having $M_{V_{max}} \simeq -10.7$. V1500 Cyg is remarkable for a number of other attributes rarely seen in classical novae (CNe). For example, during the weeks before its eruption, it showed a dramatic ∼7 mag brightening (Collazzi et al. 2009). Following eruption, the dominant photometric period declined from 0.140 d in 1975 (Semeniuk et al. 1977), to the current stable period of 0.139 62 d in 1978 (Patterson 1979). Over this interval the amplitude of the variations in its visual light curve increased to $\Delta m \sim 0.65$ mag. Even more interesting, however, were the observations by Stockman, Schmidt & Lamb (1988) that V1500 Cyg exhibited circularly polarized light, and that the polarized light curve had a period that was 2 per cent shorter than the photometric period. V1500 Cyg became the first 'asynchronous polar', where a highly magnetic white dwarf spins at rate that is slightly different from its orbital period. Unlike the intermediate polars, where the magnetic white dwarf primary also spins at a different rate than the orbital period, asynchronous polars do not appear to have accretion discs.

Continued polarimetric study of V1500 Cyg showed that the white dwarf spin period was slowly increasing, and the system would attain synchrony within a few hundred years. Initial explorations of the processes that might generate the torques necessary to create this rapid spin-down rate showed that they were at least an order of magnitude too small to match observations (Schmidt & Stockman 1991, and references therein). In contrast, Campbell & Schwope (1999) found that the torque resulting from induced electric fields and current flow in the secondary star from an asynchronous magnetic white dwarf could explain the spin-down time-scale for V1500 Cyg. In their modelling, if the white dwarf had a mass of 0.5 $M_\odot$, the spin-down time-scale was of the order of 50 yr. If the white dwarf mass was higher than this, the spin-down time-scale would be longer. Given the violence of the CNe eruption of V1500 Cyg, and the presence of a modest enhancement of neon in its ejecta, it is assumed that the mass of the white dwarf in the system is large (Lance, McCall & Uomoto 1988; Politano et al. 1995).

Without adequate knowledge of many important system parameters, it is difficult to assess the viability of any magnetohydrodynamic torque model that attempts to explain the spin-down rate of V1500 Cyg. To enable more robust models requires measurements of the current spin rate, the current mass accretion rate, an estimate of the orientation of the magnetic field with respect to the binary orbit, and limits on the magnetic field strength of the primary. Since the accretion regions of magnetic cataclysmic variables (CVs) are sources of high-energy photons, X-ray observations of such objects can be used to directly measure the white dwarf spin period with little ambiguity. Such data can also provide limits on the accretion rate, and often allow some constraints on the accretion geometry. When these data are combined with co-temporal optical and infrared light curves, there is the possibility of additional insight into the properties of the system.

Harrison, Campbell & Lyke (2013b) showed that the partial *XMM* light curve of V1500 Cyg was indicative of a brightening that was consistent with the behaviour expected of a polar accretion region. We have obtained new *XMM* observations that cover four orbital cycles of V1500 Cyg and these reveal a strong, periodic brightening once per orbit. Period estimation techniques applied to the X-ray data suggest that the current white dwarf spin period is very close

★ E-mail: tharriso@nmsu.edu

to the orbital period. When we combine this result with new optical and near-IR photometry, we conclude that the white dwarf in V1500 Cyg appears to have achieved synchronization, and is again a true polar. In the next section we describe the data reduction process, in Section 3 we model the X-ray and ground-based data; we discuss the results and our conclusions in Section 4.

## 2 DATA

We have obtained both X-ray and *U*-band data for V1500 Cyg using *XMM*. We have also used the New Mexico State University (NMSU) 1 m telescope to obtain *BVRI* light curves, and Near-Infrared Camera and Fabry-Perot Spectrometer (NIC-FPS) on the Astrophysical Research Consortium (ARC) 3.5 m telescope at Apache Point Observatory to obtain near-infrared photometry. We elaborate on these data sets here.

### 2.1 *XMM* data

V1500 Cyg was observed with *XMM–Newton* beginning at 2014-11-11 13:35:11 UT, and was monitored continuously for 53.3 ks. *XMM* (Lumb, Schartel & Jansen 2012) consists of three co-aligned grazing-incidence mirror assemblies that feed the European Photon Imaging Camera ('EPIC'), and two reflection grating spectrometers (the 'RGS'). *XMM* is also equipped with a co-aligned optical monitor ('OM') for obtaining UV/optical photometry. The EPIC consists of three detector arrays, one in each of the focal planes of the telescopes: the back-illuminated CCD array called the 'PN', and the two front-illuminated CCD arrays called the 'MOS'. For our observations, the PN camera was set-up in 'small window' mode where just the central CCD chip is read. The MOS detectors were used in full frame mode. Due to the visual/UV faintness of V1500 Cyg, the 'thin' blocking window could be used so as to increase the S/N of this source. We used the *U*-band filter on the OM to obtain a light curve of V1500 Cyg. Given its expected brightness, along with the significant reddening to this object, 800 s exposure times were employed to insure sufficient S/N ratios for the *U*-band observations.

We used the standard reduction process for these data employing the 'Scientific Analysis System' (SAS[1]) developed specifically for *XMM*. To enable proper period searching, the data were first barycentric corrected using the SAS task *barycen*. Due to its orbit, *XMM* data can be compromised by a strong soft proton background (see Carter & Read 2007). To remove these events from our data set, the process outlined in the 'XMM-Newton ABC Guide'[2] was followed. Briefly, this process consists of using regions away from X-ray sources to identify time intervals when the data are compromised by proton flaring events, and then extracting data that exclude those time intervals. To produce the X-ray spectra presented below, only events from the screened data set were used. For producing the X-ray light curves, however, the data were simply background subtracted using an annulus around the point source extraction aperture. Fortunately, the soft proton background was relatively low throughout these observations.

### 2.2 Ground-based data

We used the NMSU 1.0 m telescope to obtain *BVRI* light curves for V1500 Cyg on 2014 August 6, and 31, and *V*-band light curves on 2007 October 20 and 21. The NMSU 1.0 m telescope at Apache Point is equipped with an E2V 2048 × 2048 CCD with standard Johnson–Cousins *UBVRI* filters. These data were processed in the normal way, and calibrated light curves for the programme object were generated using known *UBVRI* photometry for several nearby field stars listed in Kaluzny & Semeniuk (1987). We obtained *JHK* photometry of V1500 Cyg using the 'NIC-FPS' on the ARC 3.5 m telescope on 2014 August 31 and October 30. Calibrated differential photometry was obtained relative to several nearby stars that are in the 2MASS catalogue. An observation log is presented in Table 1.

**Table 1.** Observation log.

| Resource | Start time | Stop time | Wavelengths |
|---|---|---|---|
| *XMM* | 2014-11-11 13:35:11 | 2014-11-12 04:48:31 | X-ray/*U*-band |
| NMSU 1m | 2007-10-20 04:17:09 | 2007-10-20 06:58:39 | *V* |
| ” | 2007-10-21 04:12:13 | 2007-10-21 08:10:18 | *V* |
| ” | 2014-08-06 06:00:59 | 2014-08-06 10:10:14 | *BVRI* |
| ” | 2014-08-31 02:42:22 | 2014-08-31 09:34:41 | *BVRI* |
| ARC 3.5 m | 2014-08-31 03:42:13 | 2014-08-31 06:53:11 | *JHK* |
| ” | 2014-10-30 00:47:17 | 2014-10-30 04:31:15 | *JHK* |

## 3 RESULTS

### 3.1 The X-ray and *U*-band light curves of V1500 Cyg

The X-ray and *U*-band light curves from *XMM* are shown in Fig. 1. The top panel has the MOS1 (black) and MOS2 (red) data, while the middle panel has the PN light curve (the light-curve model in green will be described below). The presence of reflection gratings

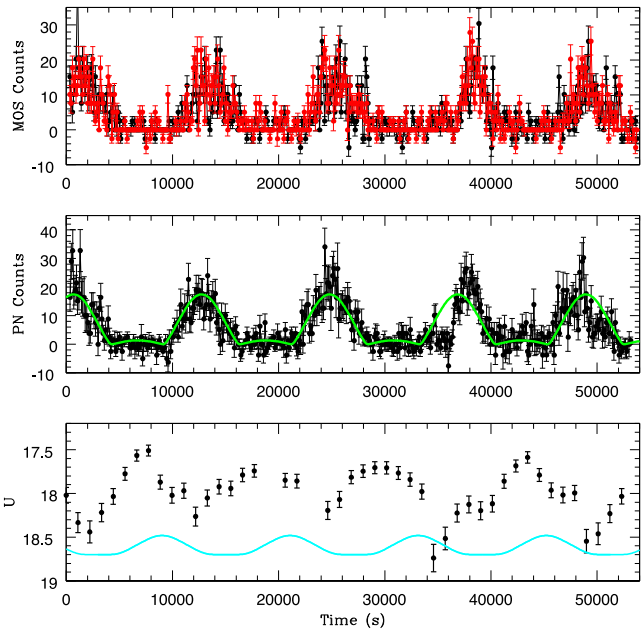


**Figure 1.** The light curves of V1500 Cyg derived from the *XMM* observations. The top panel has the MOS1 (black) and MOS2 (red) data, while the middle panel shows the PN light curve. The green curve overplotted on the PN data set is a light-curve model that was generated to explain the folded light curve (see Fig. 2) as due to two bright spots on the white dwarf primary. The changing morphology of the X-ray maxima makes absolute spin period determination difficult. The bottom panel are the *U*-band data from the OM. The solid cyan line in this panel is the light-curve model described in the text in Section 3.3.

[1] http://xmm.esac.esa.int/external/xmm_data_analysis/
[2] https://heasarc.gsfc.nasa.gov/docs/xmm/abc/abc.html

in the optical paths of the MOS detectors, to feed the RGS, is partially responsible for the lower observed count rates from these devices when compared to that for the PN. The *U*-band data are presented in the bottom panel (the light-curve model plotted in this panel will be described in Section 3.3). The long duration of the observations allowed the partial coverage of five X-ray maxima. The X-ray maxima are not symmetric, nor does their morphology repeat from one cycle to the next. The fourth X-ray maximum was much briefer, and had a faster rise to, and fall from, maximum. The 'missing' section from the early part of this brightening corresponds to the faintest part of the *U*-band light curve. Perhaps there was a pause in the mass accretion at this particular instant. Another such minimum at 49 000 s in the *U*-band light curve also corresponds to a dip in the X-ray flux. Note that the maxima in the *U*-band light curves occur during the X-ray minima, and the large excursions seen in these data cannot be directly attributed to thermal hotspot emission from the main accretion region.

We extracted a light curve from the PN event list binned into 1 s intervals and searched it for the best-fitting period using the XRONOS[3] task *efsearch*. The ephemeris of Schmidt, Liebert & Stockman (1995) would predict the spin period at the time of these observations to be $P_{\rm spin} = 11\,880 \pm 4$ s. Obviously, with temporally limited observations on a single epoch, it is difficult to determine a precise spin period. Using a range of input values for the binning inside *efsearch*, leads to ambiguous results. The period with the strongest ratio of the measured to expected variance (Var/expVar = 58) is $P_{\rm spin} = 12\,031$ s, and occurs when we use 25 phase bins per period. However, there are a wide range of statistically significant periods ranging from 12 017, to 12 048 s. The limited time series, the low S/N of the X-ray data, and asymmetries of the maxima, do not allow for a more accurate period measurement with *efsearch*. As an alternative to *efsearch*, we used the period searching, light-curve fitting software 'PERIOD04' (Lenz & Breger 2005). When input into PERIOD04, the PN light curves binned by 10 and 60 s, yield periods of 12 062 and 12 058 s, respectively. These are essentially identical to the orbital period of V1500 Cyg: $P_{\rm orb} = 12\,062.5$ s. Even without a robust value for the spin period, it is clear that the white dwarf is now much closer to synchronization than would have been predicted.

Given these results, and when analysed in conjunction with the ground-based data presented below, we believe the spin period of the white dwarf is now synchronous with the orbital period. If we fold the (1 s binned) light curve on the orbital period, we can attempt to extract other useful information. The folded PN light curve is shown in Fig. 2, where we have set phase $\phi_{\rm spin} = 0$ to be equal to the centroid of the primary maximum. Once we have folded these data, we find that there is little evidence for a secondary maximum near phase 0.5. In their polarization light curve, Schmidt & Stockman (1991) found direct evidence for two pole accretion. A weaker X-ray maximum could arise from a lower accretion rate, or due to a poor viewing geometry for this secondary pole. From the X-ray light-curve data alone, the reality of this pole cannot be established. In this way, V1500 Cyg resembles the polar BL Hyi, an object that has a very weak/rarely detected secondary X-ray pole, but one that is prominent in polarimetric light curves (see Schwope et al. 1998).

We can use the Wilson–Divinney light-curve modelling code WD2010[4] to explore possible geometries that can reproduce the pro-

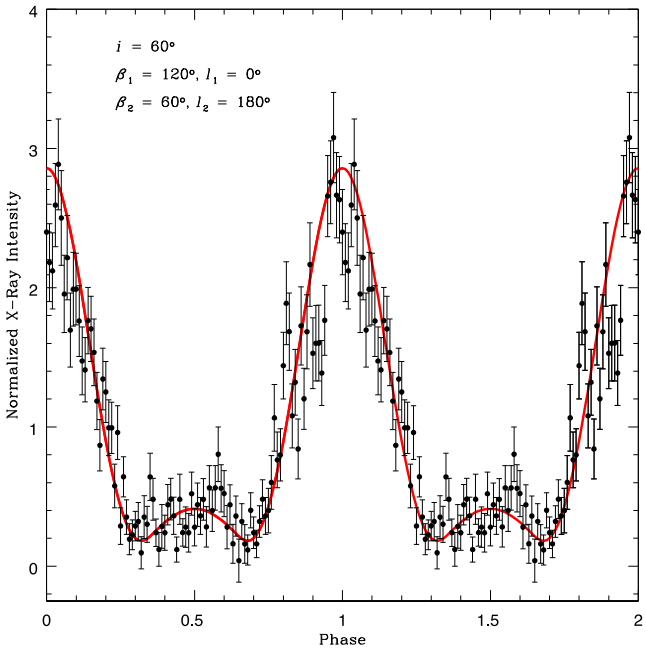


**Figure 2.** The PN light curve folded on a period of 12 062.5 s. The red line is a light-curve model that reproduces the morphology of the X-ray data set. In this model, the binary orbital inclination is 60°, and the two spots are opposite each other on the white dwarf: separated by 180° in longitude, and having co-latitudes of $\beta_1 = 120°$, and $\beta_2 = 60°$. Phase 0 here is defined as the centre of the X-ray maximum.

file of the folded light curve. Given the large number of possibilities for the input parameters in any light-curve modelling project, we need to supply some constraints to derive anything useful. As shown in Schmidt & Stockman (1991), there are two accreting poles that appear to be located on opposite sides of the white dwarf. In addition, the switch between positive and negative branches is well defined, and suggests that these regions are not visible for much more than one half of a rotation period. The spectropolarimetry presented in Schmidt et al. (1995) suggests that the duration of the negative polarization may be briefer than that for the positive polarization. The polarization data also suggest that neither pole is face-on at transit. Schmidt et al. derived an orbital inclination of $i = 60°$ that we accept for the remainder of this paper.

We start by separating the two spots by 180° in longitude. A spot with a co-latitude of $\beta = 90°$ will be visible for one half of a rotation period (or orbit here). Larger co-latitudes mean briefer transits, smaller co-latitudes produce longer transits. While there are a large number of light-curve models that play the co-latitude of the spot off against the spot radius, there are basically two families of solutions: the spots are small in size and in the same upper hemisphere (above the line of sight), or the spots are in both upper and lower hemispheres, and are much larger. If both spots were to have $\beta < 60°$, they would remain visible at all times, producing broad maxima. The optical/IR light curves discussed below appear have a sharp minimum near $\phi = 0$, suggesting that at least one of the poles disappears from view. This is also suggested by the polarization results, and thus we prefer a model where we locate one of the poles below our line of sight. In Fig. 2, we plot a model where we have two very large hotspots (radius = 45°) separated by 180° in longitude, and that have co-latitudes of $\beta_1 = 120°$, and $\beta_2 = 60°$. This large spot radius is required to generate the broad primary maximum. While the Wilson–Divinney code models these spots as

[3] https://heasarc.gsfc.nasa.gov/docs/xanadu/xronos/
[4] ftp://ftp.astro.ufl.edu/pub/wilson/lcdc2010/

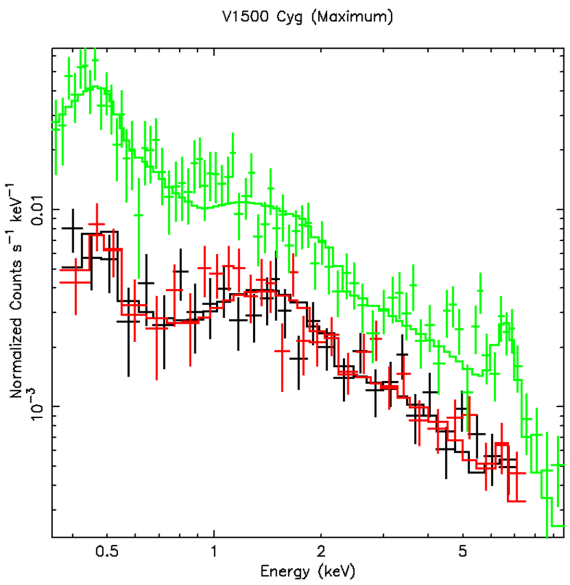


**Figure 3.** The maximum light X-ray spectra of V1500 Cyg. Green data points are from the PN, the black from the MOS1, and the red from MOS2. The solid line through each data set is the best-fitting XSPEC model for that detector, consisting of a thermal bremsstrahlung source, a blackbody, and a Gaussian line with the parameters listed in Table 2.

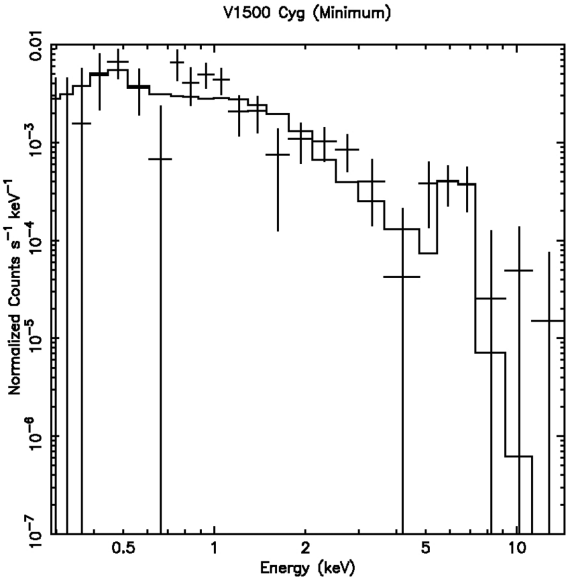


**Figure 4.** The minimum light PN spectrum of V1500 Cyg. The XSPEC model fitted to these data has a blackbody temperature of $kT_{\rm bb} = 50$ eV and $kT_{\rm tb} = 1.9$ eV, and a Gaussian line (see Table 2).

circles, a long arc of X-ray emission oriented in longitude could also reproduce a broad maximum. Note that we have set $\beta_2 = 60^\circ$, and the secondary spot would be face-on at transit. Unfortunately, the location of this spot is impossible to constrain given the low count rate.

### 3.2 The X-ray spectra of V1500 Cyg

To extract X-ray spectra for V1500 Cyg, we rigorously screened the X-ray data for proton events by constructing 'good time' intervals free of such contamination. We then further delineated regions containing the X-ray maxima and minima from this screened event list to extract spectra for both phase intervals. The spectra for the X-ray maxima are shown in Fig. 3, and that at light curve minimum in Fig. 4. Due to the very low count rate during minimum, only the PN data were extracted, and they had to be heavily binned to achieve a spectrum that could be modelled. We constructed model spectra using XSPEC[5] with three emission components consisting of a soft blackbody, a thermal bremsstrahlung source, and an emission line, all absorbed by a hydrogen column. As discussed in Harrison et al. (2013b), the visual extinction to V1500 Cyg is $A_{\rm V} = 1.5$ mag, leading to $N_{\rm H} = 2.5 \times 10^{21}$ cm$^{-2}$. The hydrogen column was kept 'frozen' during all XSPEC model fitting. It has been shown previously that there is often evidence for additional absorption in the X-ray spectra of polars, in step with the orbital period (cf. Wolff, Wood & Imamura 1999), and often attributed to the accretion stream and the changing viewing geometry. We do not believe that our data are of sufficient quality to allow this parameter to be unconstrained during modelling, nor to search for possible orbital modulations.

We chose a simple three component model as it a typical spectrum for high state polars (see Beuermann, El Kholy & Reinsch 2008). The best-fitting model has a thermal bremsstrahlung source with $kT_{\rm tb} = 100$ keV, and a soft blackbody source with $kT_{\rm bb} = 60$ eV, resulting in $\chi^2_{\rm red} = 1.03$. With $kT_{\rm tb}$ fixed, both cooler *and* hotter values for the blackbody component result in poorer fits. For example, setting $kT_{\rm bb} = 40$ eV, gives $\chi^2_{\rm red} = 1.25$, while $kT_{\rm bb} = 80$ eV results in $\chi^2_{\rm red} = 1.13$. The very high temperature of the thermal bremsstrahlung component is not well constrained due to the lack of sufficient hard photons in the X-ray data. For example, setting $kT_{\rm tb} = 30$ keV (with $kT_{\rm bb} = 60$ eV), leads to $\chi^2_{\rm red} = 1.09$, while $kT_{\rm tb} = 40$ keV gives $\chi^2_{\rm red} = 1.06$. These lower values for the temperature of the thermal bremsstrahlung component in V1500 Cyg are more in line with those observed for the typical polar in a high state (see Warner 1995; Christian 2000; Landi et al. 2009). The final model spectrum, listed in Table 2 and plotted in Fig. 3, has $kT_{\rm tb}$ = 40 keV and $kT_{\rm bb}$ = 60 eV. We conclude that during the bright phases, the X-ray spectrum of V1500 Cyg is similar to, but possibly hotter than, the typical high state polar.

The X-ray flux during the minimum light phases is very low, making its spectrum harder to constrain. With $kT_{\rm bb}$ fixed at 60 eV, we find the best-fitting thermal bremsstrahlung component has $kT_{\rm tb} = 2.1$ keV ($\chi^2_{\rm red} = 0.96$). If we let both temperatures be free, the best-fitting XSPEC solution has $kT_{\rm bb} = 132$ eV, and $kT_{\rm tb} = 11.7$ keV ($\chi^2_{\rm red} = 0.88$). In either scenario, the thermal bremsstrahlung source is much cooler during minimum light than during the X-ray maxima. Lower temperatures for the blackbody source directly lead to lower temperatures for the thermal bremsstrahlung source. A blackbody

**Table 2.** X-Ray spectral parameters.

| Component | Primary maximum | Secondary maximum |
|---|---|---|
| $N_{\rm H}$ (fixed) | $2.45 \times 10^{21}$ cm$^{-2}$ | $2.45 \times 10^{21}$ cm$^{-2}$ |
| $T_{\rm BB}$ | $60 \pm 1.3$ eV | $50 \pm 6.7$ eV |
| Normalization (BB) | $1.4 \pm 0.1 \times 10^{-5}$ | $4.5 \pm 0.3 \times 10^{-6}$ |
| $T_{\rm TB}$ | $40 \pm 9$ keV | $1.85 \pm 0.7$ keV |
| Normalization (TB) | $3.2 \pm 0.2 \times 10^{-5}$ | $7.9 \pm 0.2 \times 10^{-6}$ |
| Gaussian line energy | $6.6 \pm 0.2$ keV | $6.6 \pm 0.4$ keV |
| Gaussian line width | $0.4 \pm 0.3$ keV | $0.4 \pm 0.4$ keV |
| Normalization (line) | $2.4 \pm 0.6 \times 10^{-6}$ | $1.0 \pm 0.6 \times 10^{-6}$ |
| HJD(TDB) of maximum | $2456\,073.3731 \pm 0.0010$ | – |

[5] http://heasarc.gsfc.nasa.gov/xanadu/xspec

temperature of $kT_{\rm bb} = 50$ eV requires $kT_{\rm tb} = 1.9$ eV to achieve $\chi^2_{\rm red} = 1.08$. This is the model listed in Table 2, and plotted in Fig. 4. Even though not tightly constrained, this result does indicate the presence of a second accretion region.

Over the energy interval 0.5 to 10 keV, the peak bright phase X-ray flux is $6.3 \pm 0.5 \times 10^{-13}$ erg cm$^{-2}$ s$^{-1}$. For a distance of 1 kpc, the X-ray luminosity is $7.5 \pm 0.6 \times 10^{31}$ erg s$^{-1}$. This should be compared with the value of $1.6 \times 10^{32}$ erg s$^{-1}$ for the hard component of AM Her in a high state (Ishida et al. 1997), or $1.3 \times 10^{31}$ erg s$^{-1}$ for BL Hyi (Beuermann & Schwope 1989). Using equation (2.90) in Warner (1995), and a shock temperature of 40 keV, the lower limit on the mass of the white dwarf in V1500 Cyg is 1.13 $M_\odot$. This estimate for the mass of the white dwarf is in line with expectations, given the rapid evolution of its CNe eruption. Assuming $L_{\rm acc} = GM_{\rm wd}\dot{M}/R_{\rm wd}$, we find $\dot{M} \sim 6.6 \times 10^{14}$ gm s$^{-1}$. Thus, the spectral parameters, mass transfer rate (cf. Ramsay & Cropper 2003), and the X-ray luminosity of V1500 Cyg are consistent with a normal polar in a high state.

### 3.3 The optical/near-IR light curves

We obtained four epochs of ground-based light-curve data: *V*-band photometry in 2007 October, *BVRI* photometry on 2014 August 06, *BVRI* and *JHK* data on 2014 August 31, and *JHK* only on October 30. The *BVRI* light curves are shown in Figs 5 and 6, while the *JHK* data are shown in Figs 7 and 8. The *JHK* light curves shown here are essentially identical to those we obtained in 2006 (Harrison et al. 2013b). The 2007 *V*-band data are plotted in Fig. 9. We have extracted the *V*-band data from Semeniuk, Olech & Nalezyty (1995), and present it as Fig. 10. The morphology of the *V*-band light curve appears to have changed little since 1995, though the source has faded by nearly a magnitude. In all figures, the photometry has been phased using the minimum light ephemeris in Semeniuk et al. (1995). This precise ephemeris was established using visual data spanning nearly a decade, and at the epoch of our observations the error bars on the phasing of the minima are <0.5 per cent. In the bottom panel of Fig. 5, we combine all of the light-curve data to enhance the phase resolution by applying vertical offsets to the individual light curves to overlay them. For the August 31 data, we repeat the *V*-band panel, but with the inclusion of a light-curve model that has two large hot spots at the longitudes and latitudes of the two accretion regions found above (see Fig. 2). We will discuss this panel in Section 3.4.

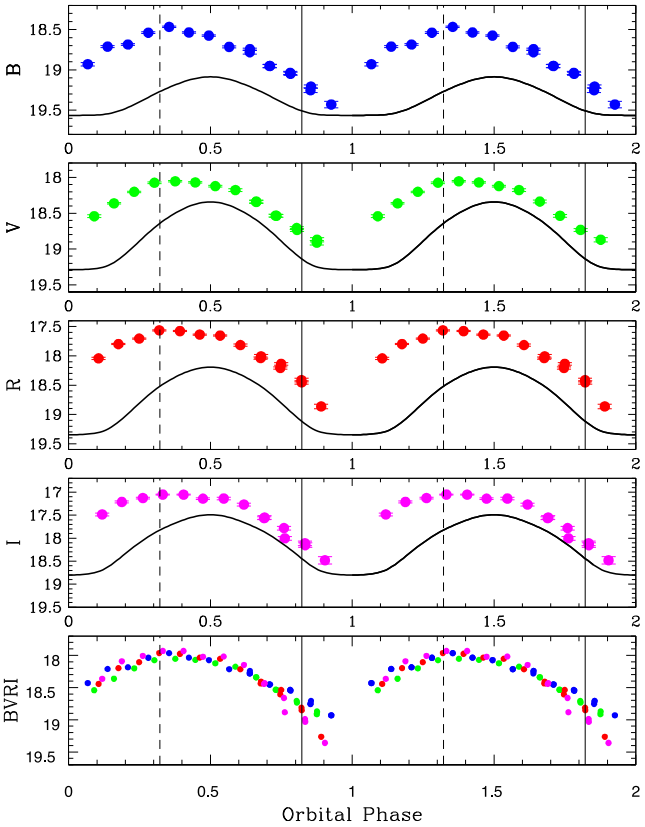


**Figure 5.** The *BVRI* light curves of V1500 Cyg for 2014 August 06. In the bottom panel, we plot all four data sets with arbitrary vertical offsets to improve the phase resolution. The solid line in each panel is the light-curve model described in the text. The solid vertical lines in each panel are the locations of the transit of the primary X-ray maximum, while the dashed lines are the transit phase of the secondary pole. These data have been repeated for clarity.

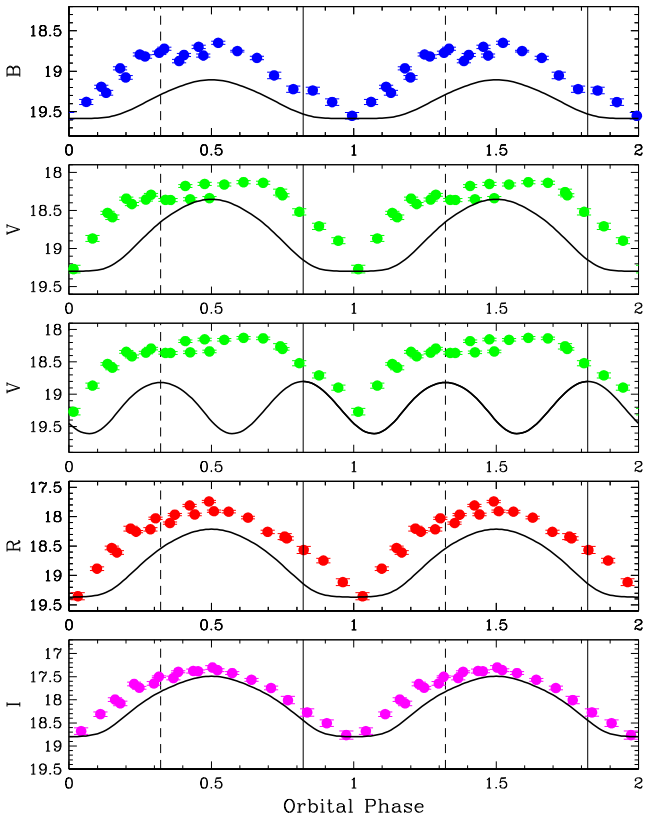


**Figure 6.** The *BVRI* light curves for August 31, as in Fig. 5, except that the *V*-band data have been repeated in the middle panel and overlaid with a two hotspot model to show the differing transit durations of the magnetic poles, see Section 3.4.

As elaborated by Schmidt et al. (1995, and references therein), the large optical modulations are believed to be due to a hot white dwarf heating a cool secondary star. They derived $T_{\rm wd} = 90\,000$ K, $T_2 = 3000$ K, and $i = 60^\circ$. As shown in Harrison et al. (2013b), such a model generates a flat-bottomed minimum. None of our light curves truly has such a flat bottom, though the *I*-band light curve on August 31 has the flattest minimum. We cannot produce a sharp minimum in light-curve models, regardless of the inclination, assuming an irradiated secondary star. The complexity of the

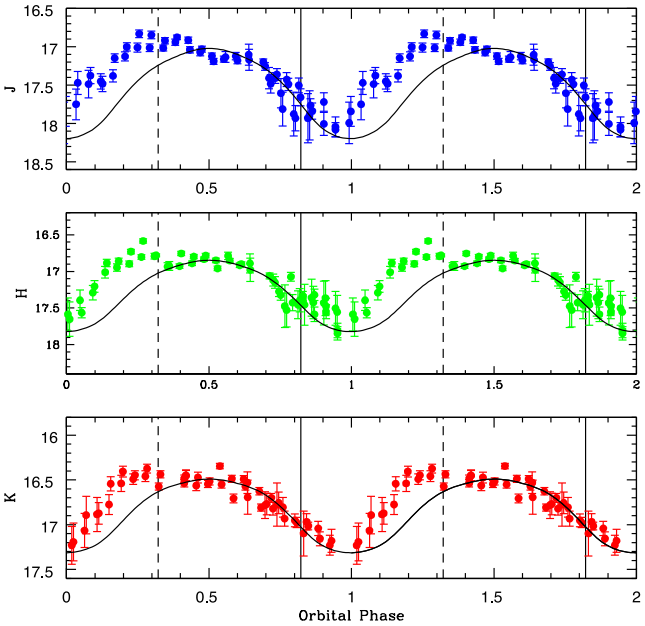


**Figure 7.** The *JHK* light curves for 2014 August 31. The solid line in each panel is the irradiated secondary star light-curve model described in the text. As in the previous figures, the phases of accretion region transits are identified.

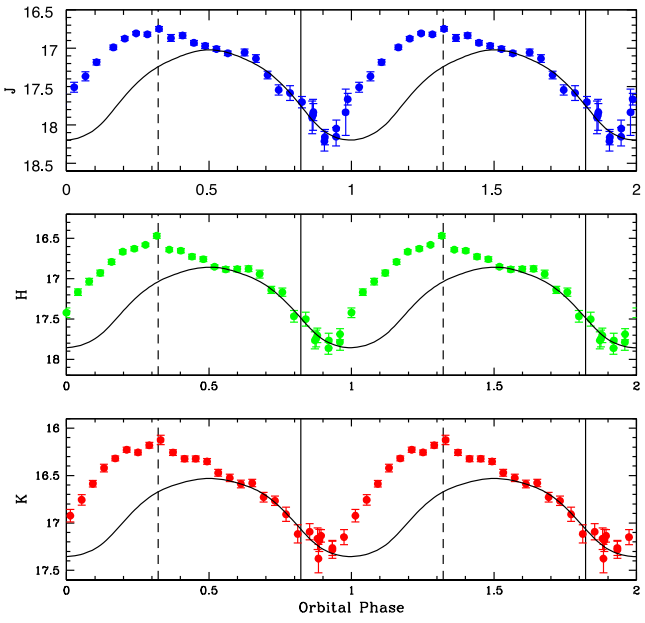


**Figure 8.** The *JHK* light curves of V1500 Cyg for October 30 as in Fig. 7.

*V*-band light curves suggests additional emission components in the binary system. The two epochs of *JHK* data were similar, though the August 31 data set was plagued by poor seeing near $\phi = 0$. Morphologically, they are essentially identical, though the large excess from $\phi$ =0 to 0.5 seen in the October 30 data appears to be somewhat smaller on August 31. We focused our modelling effort on trying to simultaneously match both the *I*-band data for August 31 and the October 30 *JHK* light curves with only an irradiated secondary star model.

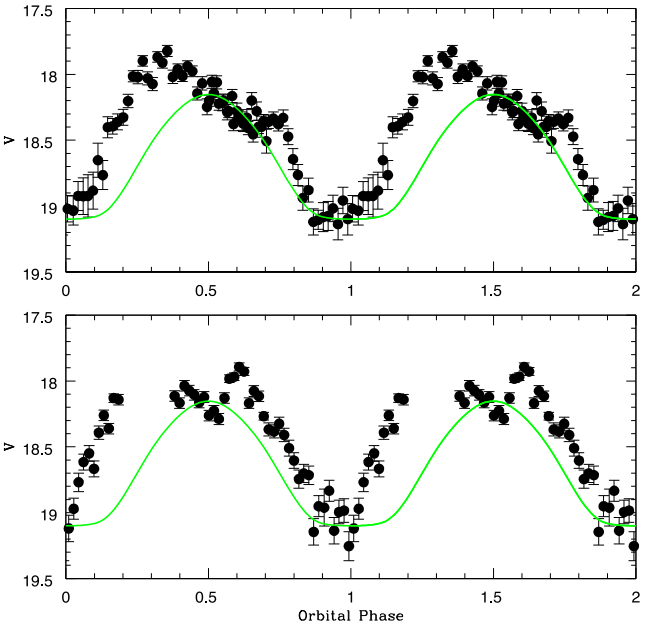


**Figure 9.** The *V*-band light curve of 2007 October 21 (top), and for October 20 (bottom). The solid green line in both panels is the irradiated secondary star model described in the text, offset by $\Delta\ V = -0.2$ mag. The light curve for October 20 is incomplete, with a gap between phase 0.2 and 0.4.

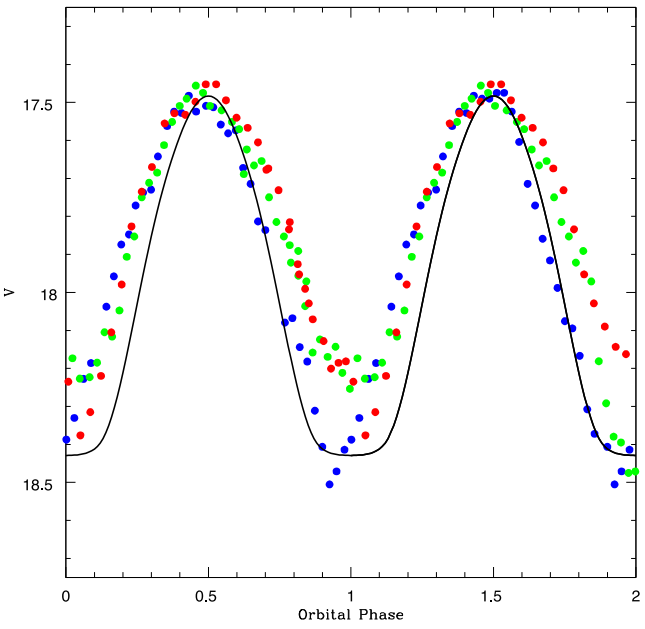


**Figure 10.** The *V*-band light curves of V1500 Cyg in 1995, extracted from Semeniuk et al. (1995), and phased to their minimum light ephemeris. Data for July 27 are plotted in blue, July 28 in green, and July 29 in red. The data for July 27 have been offset by $\Delta V = -0.18$ mag, and those for July 28 have been offset by $\Delta V = -0.05$ mag, to achieve maxima that agree with that for July 29. The irradiated secondary star model discussed in the text is plotted as the solid line, after being offset by $\Delta$V = −0.87 mag.

We ran WD2010 over a wide range of temperature and inclination (including the appropriate wavelength-dependent light-curve modelling parameters required by the Wilson–Divinney code, see Harrison et al. 2013a). We settled on a model with $T_{\rm wd} = 52\,000$ K, $T_2 = 3100$ K, and $i = 60^\circ$. As can be seen in the plots, this model reasonably fits the *I*-band data for August 31, and appears to

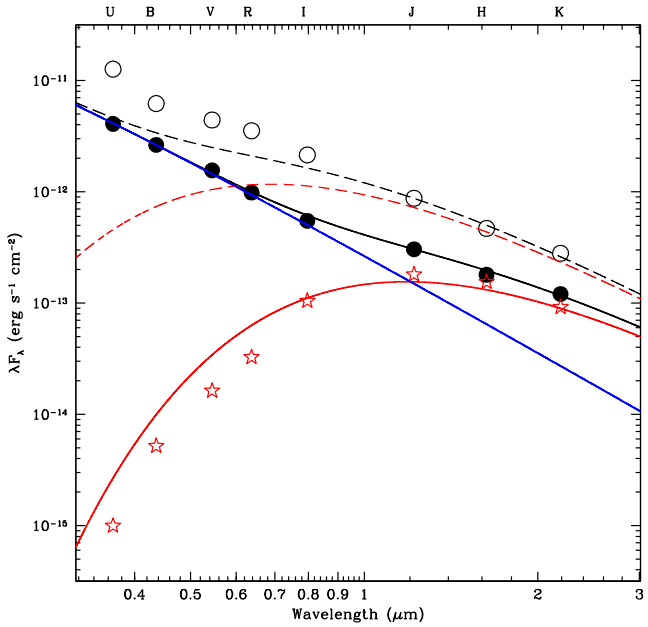


**Figure 11.** The spectrum of V1500 Cyg at $\phi = 0$ (solid circles and lines), and $\phi = 0.5$ (open circles, dashed lines). The data for minimum light have been fitted with a two blackbody model comprised of a hot white dwarf ($T_{\rm eff} = 52\,000$ K, blue), and a cool secondary star ($T_{\rm eff} = 3100$ K, red). The sum of both components is plotted as a black solid line. The data for $\phi = 0.5$ have also been fitted with a two blackbody, but now the cooler component has $T_{\rm eff} = 5300$ K (red dashed line). The sum of the hot white dwarf and the hotter hemisphere of the irradiated secondary star is plotted as a black dashed line. The *BVRI* excesses at this phase are apparent.

perfectly explain one half of the *JHK* light curves (over $0.5 \leq \phi \leq 1.0$). While we could adjust the model parameters, such as the inclination, so that it could fully explain the *I*-band maximum, we felt that the deviation from the irradiated model on either side of minimum in this bandpass indicated that there was excess emission present at all phases. There is a large excess in the near-infrared light curves from $\phi = 0$ to $\phi = 0.5$. There is a significant excess above the irradiated secondary star model *at nearly all phases* in the *UBVR* data. We also plot this model, offset by $-0.2$ mag, on to the *V*-band light curves of 2007 October shown in Fig. 9. The higher temporal cadence of the 2007 October 21 *V*-band data reveals an excess above the light-curve model that is almost identical in amplitude and morphology to the *JHK* excesses seen in 2014 October. The data on October 20 find larger pre- and post-maxima excesses, though the light-curve model passes through the photometry near phases 0.0 and 0.5.

Since the light-curve models are normalized to fit the data, we need to examine the spectral energy distribution (SED) to insure that our model is realistic. In Fig. 11 we plot the *faintest U*-band data point from the *XMM* light curve, the August 31 *BVRI* data, and the *JHK* fluxes at phase 0.0. The solid circles in this plot are the minimum light data, and have been fitted with the sum of two blackbodies: $T_{\rm bb_1} = 52\,000$ K + $T_{\rm bb_2} = 3100$ K. The resulting SED is consistent with the observed data at light curve minimum with only the stellar components as sources of luminosity. Note that for an M4V ($T_2 = 3100$ K) to explain the spectrum requires a distance of 1 kpc to V1500 Cyg. The Wilson–Divinney code also predicts the luminosity of the white dwarf in each of the modelled bandpasses. For the hot blackbody to reproduce the observed *V*-band flux also requires $d \sim 1$ kpc. Lance et al. (1988) have summarized the distance estimates for V1500 Cyg and conclude that $1.2 \pm 0.2$ kpc is a reasonable mean. Note that more recently, Slavin, O'Brien & Dunlop (1995) found a distance of 1.5 kpc for V1500 Cyg from a nebular expansion parallax measurement. As shown in Harrison et al. (2013c), when compared to actual parallaxes, the secondary distance estimation techniques for CNe are not reliable. In the four cases examined, only the nebular expansion distance for GK Per agrees with its astrometric distance. For DQ Her, the nebular expansion parallax is 40 per cent larger than its true distance. Thus, if we assume $d = 1$ kpc, our light-curve model reproduces the observed spectrum at phase 0. If, of course, the distance to V1500 Cyg is 1.5 kpc, the light-curve model would need to be scaled downward by 0.9 mag, resulting in very large excesses in every bandpass and at all phases of the orbit.

It is important to mention that Barman, Hauschildt & Allard (2004) used PHOENIX atmosphere models to explore the process of heavily irradiating a CV secondary star just like that found in V1500 Cyg. Instead of the typical bolometric albedo of 0.5 used for convective stars in light-curve modelling (as used here), they found a much higher value of ≈0.8 for scenarios like V1500 Cyg. Essentially, the irradiation of the convective star makes it appear to be more like a non-convective star, and thus the bolometric albedo is closer to the value (1) found for such stars. If we set the bolometric albedo to 0.8, then we have to lower the value for the inclination to $i = 35^\circ$ to reproduce the *IJHK* light curves. Horne & Schneider (1989) argue that the strong orbital modulation in both the continuum and the emission lines, and the lack of an eclipse, constrain the inclination to be $40^\circ \leq i \leq 70^\circ$. If we use our lower limit on the white dwarf mass derived from the shock temperature, the estimated orbital inclination from their fig. 14 is $i > 50^\circ$. Similar limits were derived by Schmidt et al. (1995).

Returning to the SED of V1500 Cyg at $\phi = 0.5$, the *UBVRI* data have excesses above the irradiated light-curve model, but *J* through *K* do not. We can estimate the apparent temperature of the heated face of the secondary star using the procedure outlined in Brett & Smith (1993), and find $T_2 = 5300$ K. When we add a blackbody with this temperature to the same hot blackbody used at phase 0, see Fig. 11, we can reproduce the *JHK* observations. The model SED at *I* falls 0.2 mag below the observed flux, which is the observed difference between the light-curve model and the photometry for August 31. Thus, the irradiated light-curve model remains dominant at both inferior and superior conjunctions.

### 3.4 Possible origins for the light-curve excesses

If we accept the presence of an irradiated secondary star, and assume the white dwarf spin is now synchronized with the orbital period, we can attempt to explore the origin of the strong excesses seen in the light curves. Using the time of X-ray maximum listed in Table 2 (this is the time of the centroid of the third maximum), we can predict its phase position in the other light curves. In Figs 5 through 8, we delineate the locations of the primary (solid lines) and secondary (dashed lines) X-ray maxima for the *BVRI* and *JHK* light curves. The primary X-ray maximum, presumably when we have the most direct view to the accretion region, occurs at binary orbital phase $\phi = 0.822$, leading the secondary star around the orbit. This is the configuration observed for most polars (e.g. Cropper 1988). Examination of Fig. 8 shows that the large near-IR excesses (above the light-curve model) are not centred on the transit of either accretion region. There appears to be a small peak, or inflection point, in all three infrared bandpasses at the phase when we have our best view of the secondary pole. However, the bulk of the

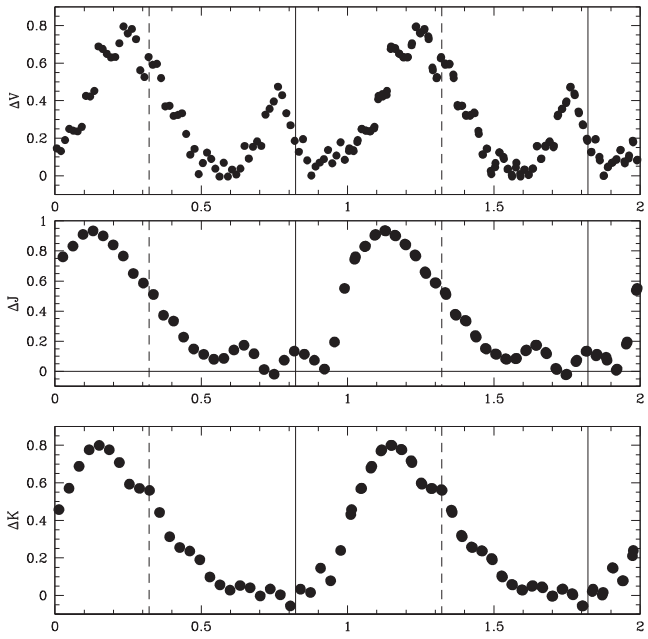


**Figure 12.** The difference plot, where we have subtracted the irradiated secondary star model from the *V*-band data for 2007 October 21, and from the *J*- and *K*-band data for 2014 October 30. The locations in phase of the transits of the two accretion regions are identified.

excess occurs before this pole reaches the centre of the disc, and quickly weakens as it rotates away. In Fig. 12, we subtract[6] the light-curve model from the *V*-band data for 2007 October 21, and from the *J*- and *K*-band light curves on 2014 October 30. The peaks in the excesses in the *V* band are close to, but not quite centred on, the transit of the two accretion regions. The excesses in the near-IR are skewed relative to the secondary pole, and reach their greatest deviation well before the accretion spots are centred on the facing hemisphere of the white dwarf. It is important to note that the same excess in the *V*-band data for 2007 October 20 began earlier, and was substantially larger, than that for October 21, and more closely resembled those seen in the near-IR. In the middle panel in Fig. 6, we plot the light curve of two round spots of identical temperature, at the locations derived from the X-ray observations (note that this model is only for the visualization of the accretion pole positions). The secondary pole is in the hemisphere above the viewing plane, and thus is visible for longer than the primary pole; it remains visible for the entire orbit, though grazing the horizon at times. The rise in the excess shortly after the minimum near $\phi = 0$ suggests that the excesses seen in *BVRIJHK* over the interval $0.0 \leq \phi \leq 0.5$, originate from the secondary pole. If we trust the normalization of the irradiated secondary star model, the primary pole does not produce a significant excess in the near-IR. This is true for all three epochs of *JHK* light-curve data. This is not the case in the visual: there is a strong excess in *BVR* in the phase interval $0.5 \leq \phi \leq 1.0$. This excess is highly variable compared to that associated with the secondary pole. In Fig. 13, we have subtracted the light-curve model from the *UBVRI* photometry. It is clear that we now have an excess in all the visual wavebands that can be associated with the primary pole. This excess is weakest in *I*, and strongest in *U*

[6] We have used IRAF to perform this subtraction, and thus many of smaller fluctuations seen in the actual light-curve data are removed due to the interpolation process used inside IRAF.

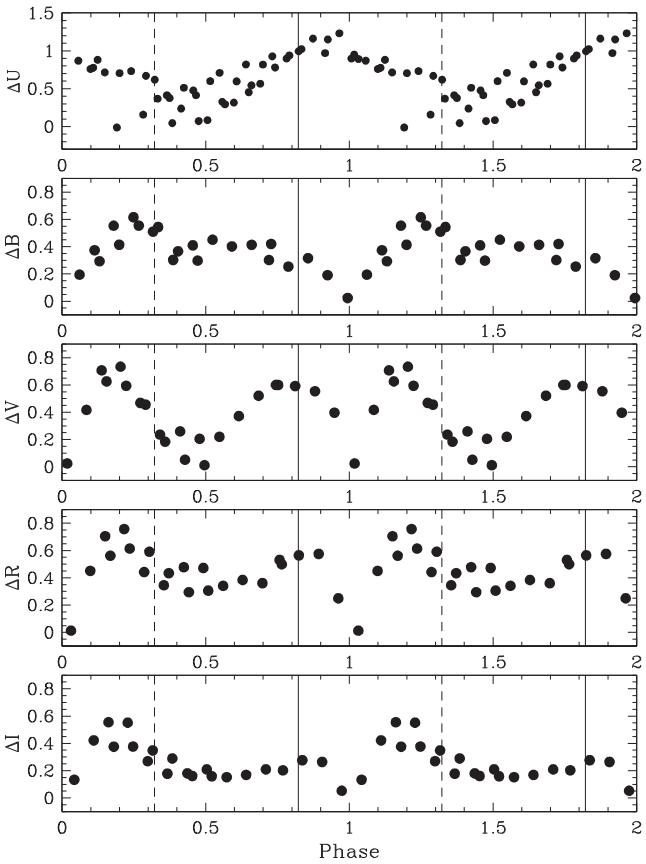


**Figure 13.** A difference plot for the *UBVRI* data for 2014 August 31 as in Fig. 12.

and *V*. The *U*-band data reveal a minimum near the time when the secondary pole transits our line of sight.

As discussed in Schmidt et al. (1995), the most likely source for the optical/IR excesses is cyclotron emission and/or emission from the accretion columns. The fact that the *U*-band reaches a maximum near $\phi = 0$, when both accretion regions are near the limb, shows that two hot blackbody sources on the white dwarf photosphere are not responsible for the excesses seen in this bandpass. If such sources are not apparent in the *U* band, they will be even less significant at longer wavelengths. As shown in Harrison & Campbell (2015, their fig. 6), the majority of the flux from optically thin cyclotron emission from the fundamental harmonic is beamed along the axis of the magnetic field, while the higher harmonics emit the majority of their flux perpendicular to field. As the temperature and/or optical depth increase, the emission from the fundamental becomes much more aligned with the field axis, with much less emission in the perpendicular direction (and, to a lesser extent, this trend is also seen for the higher harmonics). Since the optical/IR excesses are near maximum when the viewing angles to the two poles are relatively low, optically thick cyclotron emission is the leading candidate for the observed excesses.

We do not believe that emission from the accretion stream/funnel is as viable an explanation for the light-curve excesses. The main reason is that at no time have we observed an excess in the near-IR in the phase interval $0.5 \leq \phi \leq 1.0$, while the visual data show a strong, and variable excess during this time. A free–free emission source that is strong in the visual, would be strong in the near-infrared (see Harrison 2014). The opposite is true for the phase interval $0.0 \leq \phi \leq 0.5$: the strong excesses seen in the visual *are* seen in

the near-IR. If we consider the same mechanism to be responsible for both excesses, as suggested by the similar morphologies of the differenced light curves, this then rules out dilution by the stellar components as the cause for diminished free–free emission from the primary pole region at longer wavelengths. Another inference for ruling out the accretion stream/funnel is provided by the constraint derived by Schmidt et al. that the source of additional flux over the wavelength interval 1600 Å $\leq\lambda\leq$ 7000 Å, had a luminosity of $\sim$0.25 $L_{\odot}$, or about 5 per cent of the luminosity of the white dwarf in 1992. Schmidt et al. found that they could probably explain the origin of the excess they observed with clumpy, large $\dot{M}$, optically thick accretion columns that intercept and re-radiate 5 per cent of the system's luminosity. However, the current peak *B*-band excesses have relative luminosities that are 50 per cent that of the system in this bandpass.

### *3.4.1 A cyclotron interpretation for the excesses*

In the possible locations for the accretion regions discussed above, the two scenarios were that either both spots remain visible at all times, or the primary pole is located at a co-latitude that is below our sight line, while the secondary pole is visible for nearly the entire orbit. We now attempt to reconcile the light curves with a cyclotron interpretation, starting with the excesses observed in the phase interval $0.0\leq\phi\leq0.5$, which we associate with the secondary X-ray pole. A cyclotron model for these excesses needs to explain the following light curve features: (1) the near-IR excess turns on near $\phi=0.0$, (2) the excess is not at its strongest when the secondary accreting pole is near the limb, (3) the excess is largest as the secondary pole rotates towards transit, but drops as the spot transits, (4) the excess rapidly declines after spot transit, disappearing before the X-ray spot is self-eclipsed, and (5) the excesses have slightly different morphologies in different bandpasses.

A small accretion region located at $\beta<60^{\circ}$ would be visible for most of the orbit, and thus the light curve of the cyclotron emission would be broad, and slowly changing. As the pole rotated beyond the limb, possibly suffering a brief self-eclipse near antitransit, the orientation of the field lines would result in the majority of the cyclotron emission being radiated away from the observer. We have modelled this case, using the constant-$\Lambda$ cyclotron code discussed in Harrison & Campbell (2015). The light curve for a cyclotron model with $B=80$ MG, $T=10$ keV, $\Lambda=5$, $\beta=60^{\circ}$, and $i=60^{\circ}$ is presented in Fig. 14. Note that the phasing in this diagram has $\phi=0$ at spot transit. The cyclotron emission turns-on as soon as the pole is on the limb, and disappears as it rotates beyond the limb. There is a dip in all of the bandpasses at the time of transit. Obviously, this cyclotron model has little in common with the observed light curves, except that the excesses behave in a similar fashion in all of the bandpasses. Every cyclotron model, regardless of the co-latitude of the spot, or value for the orbital inclination, will have symmetric emission around the time of pole transit. Thus, such models cannot explain the skewed excesses seen in the light-curve data.

As discussed in Beuermann, Stella & Patterson (1987), if a field line is offset from the magnetic axis by an angle $\theta$, the field line is tilted from the radial direction by $\sim\theta/2$. Here, we investigate what the cyclotron model would look like if we tilt the field lines (in longitude only). A model with a tilt of 20°, corresponding to a phase offset of 40° ($\Delta\phi=0.11$), is plotted in Fig. 15. The main result is that the duration of the cyclotron excess is shortened by about 0.1 in phase. The minima near transit seen for the unbent field line model are no longer significant, as the viewing angle at this time is

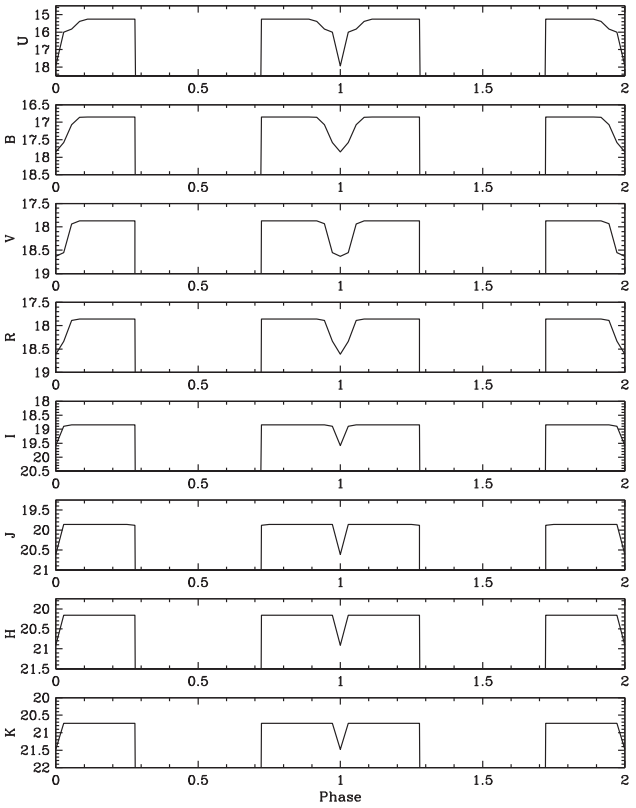


**Figure 14.** The multiwavelength light curves generated by a constant-$\Lambda$ cyclotron model with $B=80$ MG, $T=10$ keV, $\Lambda=5$, $\beta=60^{\circ}$, and $i=60^{\circ}$ over two rotational cycles.

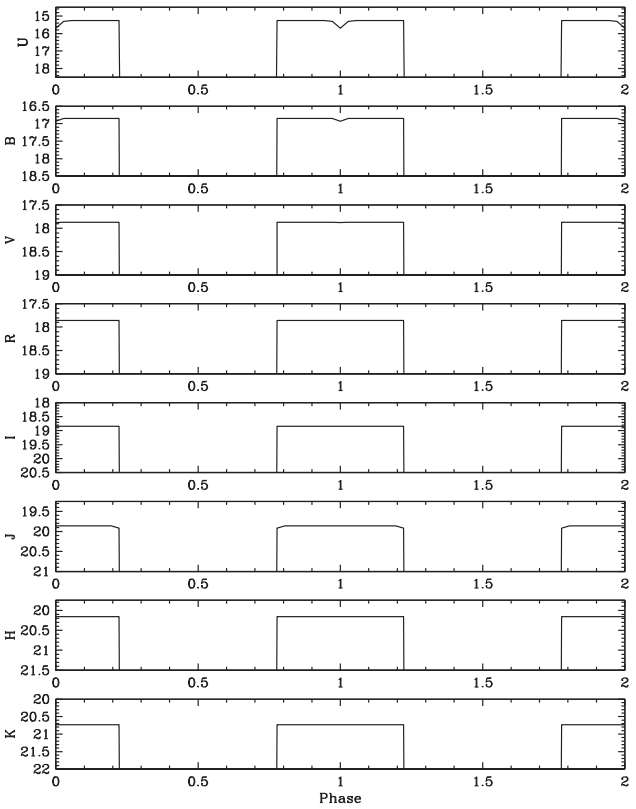


**Figure 15.** A cyclotron model as in Fig. 13, but with field lines tilted by 20°.

non-zero (20°). This leads us to propose that both accretion regions have a core-tail type distribution (cf. Cropper 1986), with the tail aligned in the direction of rotation. Regions in the tail, being located well away from the main accretion region, could have sufficiently bent field lines so as to reduce the duration of the time of maximum emission, while also peaking before transit. This would produce a heavily skewed excess, that begins to rapidly decline after transit as the tail rotates towards/beyond the limb. To explain the light curves requires that the cyclotron emission from the actual X-ray pole has to be much lower than that from the tail.

In producing the cyclotron model for the secondary pole, we specifically chose parameters so that the emission would be similar in each of the bandpasses. To explain similar visual and near-IR excesses requires a field strength near 80 MG, and a high optical depth. For $B = 80$ MG, and $\log\Lambda = 5$, the $n = 1$ cyclotron fundamental harmonic supplies similar fluxes in all three near-IR bands, while the $n = 2$ and 3 harmonics produce the visual excesses. Field strengths much different from 80 MG, cannot easily reproduce the observations for the secondary pole as the cyclotron fundamental moves out of the *J* (*B* lower) or *K* (*B* higher) bandpasses. A much lower field strength near 27 MG can result in somewhat similar *JHK* light curves, but with differing, deeper minima at transit due to this emission coming from different harmonics in *J* versus *K*. The excesses in the visual from such a field are substantially weaker, as they result from higher harmonics (e.g. 7 and 8 for the *V*-band), and would require much hotter temperatures to pump them up to a level sufficient to explain the bluer excesses. Also note that the field strength at the X-ray poles has to be slightly higher than those in the tail. For example, a region with $B = 80$ MG located 20° from the pole implies that the field strength at the pole would be $B \sim 85$ MG (see Achilleos & Wickramasinghe 1989). Obviously, the expectation is that the tail region would consist of a gradient of field strengths and field angles, allowing for a complex light-curve morphology.

An alternative scenario is to suppose that there is another accreting pole located close to the secondary pole, but one in which the accretion rate is lower, and the cyclotron optical depth is lower. Like the previous model, we propose that the secondary X-ray accreting pole does not strongly emit cyclotron emission. If the cyclotron-emitting pole is located $\Delta\phi = 0.18$ ahead of the X-ray pole, it easily explains the observational constraints. In addition, the symmetry of the excess is better explained by such a model. There remains a slower rate of decline of the excess after X-ray pole transit, which could be attributed to a small amount of cyclotron emission coming from the X-ray pole. The different light-curve morphologies in the various bandpasses can also be more easily explained by cyclotron emission from two poles with different conditions, visibilities, and field strengths.

We do not have as tight of constraints on the phasing of the excesses associated with the primary pole since there is no emission above the light-curve model in the near-IR, and our temporal resolution and coverage in the optical data are not as complete. In fact, the excesses shown in Fig. 13 for *BVRI* are reasonably symmetric about the transit of the primary pole. While a skew in the *V*-band excess in the interval $0.5 \leq \phi \leq 1.0$ is apparent in Fig. 12, it is smaller than the excess that occurs 0.5 phase later. Clearly, a core-tail or two accretion pole model like that evolved for secondary pole provides a better match to the data than a single isolated cyclotron source. The *V*-band excess for 2007 October 20 turns on near $\phi = 0.55$, just after the primary pole appears from behind the limb. The excess disappears when the primary pole becomes self-eclipsed. If the cyclotron emitting pole was offset by an identical amount from the primary X-ray pole as that for the secondary X-ray pole, it would transit at $\phi = 0.64$, in agreement with the observed offset.

The uniformity of the excesses across the optical/IR bands suggest optically thick cyclotron emission. For the secondary X-ray pole, using a constant-$\Lambda$ cyclotron model (see Harrison & Campbell 2015), emission from an 80 MG field could explain the lack of strong wavelength dependence, whether in an extended tail, or from an additional, discrete pole. The field strength for the primary pole accretion region must be substantially higher than that for the secondary pole. To explain the lack of cyclotron emission in the near-IR requires field strengths of $B \geq 120$ MG. The excesses in the visual bands for the primary pole are weaker than those for the secondary pole, suggesting a source with higher optical depth, and weaker cyclotron emission. This result is in agreement with one of the early predictions from modelling the accretion regions of polars: if either the mass accretion rate or magnetic field strength are increased, cyclotron emission is suppressed vis-*à*-vis bremsstrahlung emission (Lamb & Masters 1979).

Schmidt et al. (1995) present results from optical spectropolarimetry that show that the circular polarization remains positive over the phase interval $0.99 \lesssim \phi \lesssim 0.56$, but is negative only over the range $0.67 \lesssim \phi \lesssim 0.90$. At the epoch of the spectropolarimetry, the spin and orbital phases differed by $\Delta\phi = 0.06$. In the geometry and synchronized phasing that we have derived, the centres of these two polarization ranges are very close to being co-located with the two X-ray poles (note that the temporal resolution of the spectropolarimetry was quite low). This than associates the positively polarized emission with the secondary X-ray pole, and the negatively polarized emission with the primary pole.

### 3.4.2 *The V-band light curves of 1995*

It is worthwhile to more closely examine the older *V*-band light curves obtained by Semeniuk et al. (1995). Those data, presented in Fig. 10, were obtained on three different nights, and we have offset the individual light curves so that all of their maxima have similar values. We also plot the irradiated secondary star model that we derived above, offset by $\Delta V = -0.87$ mag, so it is consistent with the maxima of these data. The result is somewhat surprising: both the pre- and post-minima excesses seen in the recent data are present in these earlier epoch observations. The data for July 27 closely follow the light-curve model from phase 0.5 to phase 1.0. While on the following two days there was a large excess during this phase interval. The excess from $0.0 \leq \phi \leq 0.5$ is much more stable. This is exactly the same trends observed in our more recent visual photometry. Note that the excesses in 1995 are much smaller relative to the model when compared to the data obtained in 2007 and beyond. This can be easily explained by dilution since the source was a factor of two more luminous in 1995.

If these *V*-band excesses are truly tied to the accretion regions on the white dwarf as we argue above for the current time, the similar appearance of the older *V*-band data would suggest that V1500 Cyg was synchronously rotating just a few years after it was shown to be asynchronous! Of course, the excesses observed in 1995 do not have to arise from the same sources as those in the current system, since the accretion rate was much higher at that time. If we do, however, propagate the spin ephemeris out to the epoch of the Semeniuk et al. observations, we find that the spin and orbital phases differed by 0.01 on July 27, 0.2 on July 28, and 0.36 on July 29. Currently, we believe the main cyclotron emitting regions are advanced by 0.18 on the orbital period. If the same mechanisms and

phasing existed at the epoch of these earlier data, the light curves for July 27 should have cyclotron excesses centred near $\phi_{\rm Orb} = 0.08$, and 0.58. This is not in agreement with the light curve for this date. For July 28, the excesses would have been centred near $\phi_{\rm Orb} = 0.28$, and 0.78, which is consistent with their *V*-band data. On July 29 the excesses would have been centred near $\phi_{\rm Orb} = 0.43$, and 0.93. While there is a significant excess near $\phi_{\rm Orb} = 0.93$, any excess at 0.43 is quite small. It appears unlikely that the *V*-band light curves of Semeniuk et al. are consistent with the recent data if we assume the predicted spin period at the time of their observations. Either the source of those excesses was not located at the same sites as the current emission, or the spin rate at that time was different from that predicted by the ephemeris of Schmidt et al. (1995).

### 3.4.3 *The U-band light curve*

The morphology of the *U*-band light curve remains puzzling. As noted earlier, each of the strongest dips in the X-ray light curve are reflected in the *U*-band data. This confirms that the excess in this bandpass is due to the accretion process, since the response appears to be immediate. Since we do not have another *U*-band light curve, or co-temporal optical/near-IR data, we cannot know if these data are typical, or represent a peculiar state. The only features of this light curve is the maximum at $\phi \sim 0$, and the minimum at $\phi \sim 0.5$. Neither of these phases are special in the sense of the cyclotron models evolved above, but suggest a phenomenon tied to the orbital period. But as the irradiated secondary star model plotted in Fig. 1 demonstrates, variations due to the stellar components are small at this wavelength. It is interesting that the *HST* 'Faint Object Spectrograph (FOS) Optical' light curve, which has an effective wavelength similar to the *U* band, and is plotted as fig. 3 in Schmidt et al., is essentially identical to our *U*-band data set, except that the phasing of the two light curves differ by $\Delta\phi = 0.5$ (our data are phased to the minimum light ephemeris, theirs to the maximum light ephemeris). At the time of the *HST* observations, the spin and orbital phases were offset, and the light curve maximum in the FOS data corresponds to a spin phase of $\phi_{\rm spin} = 0.35$. The definition of the spin phase is the zero crossing of the polarization curve, a longitude that is located halfway between the two poles. For the *XMM* data, this corresponds to an orbital phase of $\phi = 0.57$. A spin phase of $\phi_{\rm spin} = 0.35$ is equivalent to a current orbital phase of $\phi_{\rm orb} = 0.92$. It appears the *U*-band maxima in both data sets are consistent with falling at the same 'spin phases'. This remarkable result, barring an incredible coincidence, only arises if the white dwarf in V1500 Cyg was asynchronous in 1992, and synchronized in 2014.

What is the source of the *U*-band excess? Obviously, the light curve could bear a considerable imprint from cyclotron emission. The relatively flat region of the differential *U*-band light curve from $\phi = 0$ to 0.3, could result from a rise in the cyclotron component responsible for the optical/IR excesses at these phases, combined with a fall in the source that has its peak near $\phi = 0.95$. Thus, it is possible that no more than one half of the *U*-band excess at $\phi = 0$ is due to this unidentified source. This source could be the accretion stream/funnel, as it follows the main accretion pole around the orbit, but precedes the donor star. This source has to be prominent in *U*, but not be seen in *B*. Perhaps the additional component of the excess is due to very strong Balmer continuum emission.

## 4 DISCUSSION AND CONCLUSIONS

We have obtained a multiwavelength, multi-epoch data set for V1500 Cyg. The X-ray light curve is dominated by accretion on to a single pole, being visible for one half of the orbit. Analysis of this light curve for periodicities indicates that the white dwarf now spins at a rate close to the orbital period. Even with the uncertainties in the period searching process, *none* of the periods identified in our search were close to the predicted spin period. Folding the X-ray data suggests the presence of a second pole located opposite to the primary pole that has a much lower accretion rate and/or temperature. This result is consistent with the polarimetric observations of Schmidt & Stockman (1991) where a symmetric light curve in the circularly polarized flux was found, suggesting diametrically opposed accretion regions. Analysis of the X-ray data shows that the spectrum and luminosity of V1500 Cyg are consistent with a high state polar.

The multi-epoch optical/near-IR data we have compiled show large excesses that appear to have identical phasing over an eight year span. By using the time of X-ray maximum, and assuming the white dwarf rotates at the orbital period, we find that these excesses are consistent with cyclotron emission from a distributed accretion region, or from multiple poles. While the secondary pole is quite weak at X-ray energies, the optical/IR data require an excess associated with its location. This excess is generally larger in amplitude, and less variable than the excess associated with the primary pole. Attributing the observed excesses to cyclotron emission leads to large field strengths for both poles: $B_1 = 120$ MG, and $B_2 = 80$ MG. Broad-band photometry can only provide limited insight into the nature of a cyclotron source, but it is obvious here that the strong photometric excesses are offset in phase relative to the location of the X-ray emitting poles. The simplest explanation is to propose cyclotron emitting regions located $\Delta\phi = 0.18$ ahead of both poles. These could be either a tails of emission, or nearby accreting poles. Distributed emission from tails, or arcs, have been proposed for polar accretion regions on a number of occasions (e.g. Wickramasinghe et al. 1991; Ramsay et al. 1996; Buckley et al. 2000), and appear to be the most likely explanation for the behaviour of V1500 Cyg. Harrison & Campbell (2015) found several examples of polars (e.g. VV Pup) where cyclotron emission from two poles located close to each other on the white dwarf photosphere, but with dramatically different magnetic field strengths, were required to explain *WISE* observations.

As noted earlier, if the observed spin-down rate had remained unchanged, the white dwarf would have had a rotation period at the time of the *XMM* observations of $P_{\rm spin} \sim 11\,880$ s. Thus, either the original spin-down rate was underestimated, or there was a sudden change in the spin-down rate sometime after 1992. While the *V*-band data from 1995 superficially resemble the more recent light curves, the spin phases of the excesses seen at that time are not consistent with those observed currently. Thus, either the spin ephemeris was incorrect, or the emission process was different at the earlier epoch. The only other data set available to us to help establish limits on when synchronization might have occurred is the first, brief *XMM* data set discussed in Harrison et al. (2013b). We have extracted a light curve from the PN data set for 2002 November 2 and overplot it (red) in Fig. 16 on top of the recent *XMM* PN that was data presented in Fig. 1. The *x*-axis is now in orbital phase. To get the two data sets to overlap requires us to shift the old data by 0.22 in phase. Obviously, we cannot know if the apparent rise to maximum in the older data set has any correlation to the behaviour observed recently, but the suggestion is that V1500 Cyg was still an asynchronous system at that time.

The rapid synchronization of V1500 Cyg appears to be at odds with existing models on how rapidly the white dwarf in such an object could be spun-down. As noted above, if the mass of the

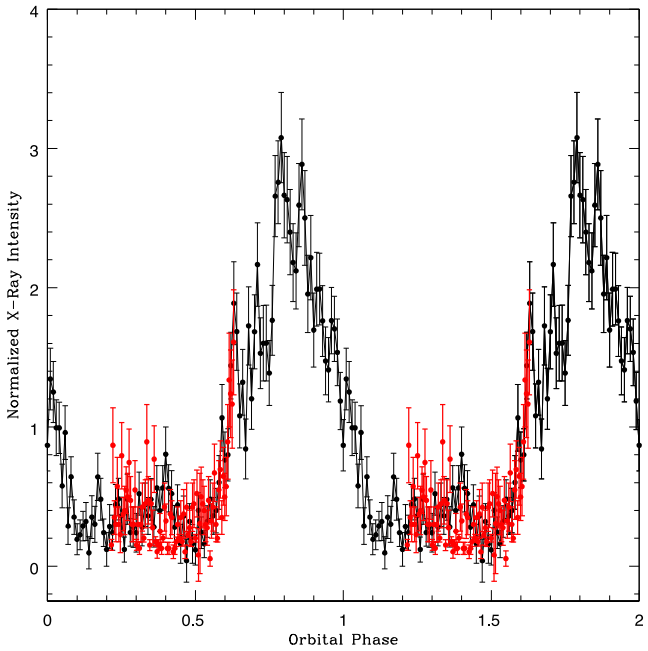


**Figure 16.** The *XMM* PN light curve for 2002 November 2 (red) overlaid on the recent PN data from Fig. 1 (black), plotted versus orbital phase. To get the older data set to align with the more recent data required an offset of $\Delta\phi = -0.22$. The 2002 data were binned by 60 s, whereas the 2014 data are binned by 120 s. The older PN data were normalized so as to best match the recent light curve.

white dwarf was low, $\leq$0.5 $M_\odot$, Campbell & Schwope (1999) predicted synchronization could occur within 50 yr by employing a torque that resulted from the currents and electric fields induced by the asynchronous rotation. That prediction is sufficiently close to be in agreement with our results. But given the violence of the CNe eruption, the probability of an ONeMg white dwarf primary, and the high X-ray shock temperatures, the primary in V1500 Cyg almost certainly has a mass that is much greater than 0.5 $M_\odot$. Thus, their mechanism might seem insufficient to explain the current observations. However, the time-scale they derive for synchronization only increases linearly with white dwarf mass, while being inversely quadratic in magnetic field strength. If the magnetic field strength of the primary pole is truly near 120 MG, the canonical synchronization time-scale is shortened by a factor of nine. Thus, the torque mechanism detailed by Campbell & Schwope would be sufficient to explain the current state of V1500 Cyg.

V1500 Cyg remains a difficult source to fully understand. It is obvious that there is a hot white dwarf that irradiates a low-mass star. The X-ray data clearly indicate a system whose spin rate is much reduced from expectations, and suggest it is close to synchronization. The recent ground-based data are also consistent with that interpretation, and suggest it has been synchronized since 2006/2007. However, it remains difficult to fully characterize the source of the optical/IR excesses. If the excesses are due to cyclotron emission, then they require either a core-tail, or a multipole geometry. A cyclotron interpretation would also argue for high magnetic field strengths for both poles. Perhaps it is these larger field strengths that aided in the more rapid spin-down observed for V1500 Cyg, when compared to other asynchronous polars such as BY Cam. Harrison & Campbell (2015) found that BY Cam had very large amplitude variations in the *WISE* bandpasses, and suggested that this was due to cyclotron emission from a field with a strength of $B \leq 28$ MG. Additional X-ray observations on several closely spaced epochs should provide for a more robust periodicity determination for V1500 Cyg. It also remains possible that discrete cyclotron harmonics might be observed from the secondary pole region, since the excesses associated with that pole are large, and do not appear to exhibit the same variations seen in the excesses that correspond to the visibility of primary pole. Such observations will be required to better constrain the field strength, and geometries of the cyclotron emitting regions.

## ACKNOWLEDGEMENTS

This was unfunded research. Based on observations obtained with *XMM–Newton*, an ESA science mission with instruments and contributions directly funded by ESA Member States and NASA. This research is partially based on observations obtained with the Apache Point Observatory 3.5-metre telescope, which is owned and operated by the Astrophysical Research Consortium. We would like to thank our anonymous referee for useful comments.

## REFERENCES

Achilleos N., Wickramasinghe D. T., 1989, ApJ, 346, 444
Barman T. S., Hauschildt P. H., Allard F., 2004, ApJ, 614, 338
Beuermann K., Schwope A. D., 1989, A&A, 223, 179
Beuermann K., Stella L., Patterson J., 1987, ApJ, 316, 360
Beuermann K., El Kholy E., Reinsch K., 2008, A&A, 481, 771
Brett J. M., Smith R. C., 1993, MNRAS, 264, 641
Buckley D. A. H., Cropper M., van der Hayden K., Potter S. B., Wickramasinghe D. T., 2000, MNRAS, 318, 187
Campbell C. G., Schwope A. D., 1999, A&A, 343, 132
Carter J. A., Read A. M., 2007, A&A, 464, 1155
Christian D. J., 2000, AJ, 119, 1930
Collazzi A. C., Schaefer B. E., Xiao L., Pagnota A., Kroll P., Löchel K., Henden A. A., 2009, AJ, 138, 1846
Cropper M., 1986, MNRAS, 222, 853
Cropper M., 1988, MNRAS, 231, 597
Harrison T. E., 2014, ApJ, 791, L18
Harrison T. E., Campbell R. D., 2015, ApJS, 219, 32
Harrison T. E., Hamilton R. T., Tappert C., Hoffman D. I., Campbell R. K., 2013a, AJ, 145, 19
Harrison T. E., Campbell R. D., Lyke J. E., 2013b, AJ, 146, 37
Harrison T. E., Bornak J., McArthur B. E., Benedict G. F., 2013c, ApJ, 767, 7
Horne K., Schneider D. P., 1989, ApJ, 343, 888
Ishida M., Matsuzaki K., Fujimoto R., Mukai K., Osborne J. P., 1997, MNRAS, 287, 651
Kaluzny J., Semeniuk I., 1987, Acta Astron., 37, 349
Lamb D. Q., Masters A. R., 1979, ApJ, 234, L117
Lance C. M., McCall M. L., Uomoto A. K., 1988, ApJS, 66, 151
Landi R., Bassani L., Dean A. J., Bird A. J., Fiocchi M., Bazzano A., Nousek J. A., Osborne J. P., 2009, MNRAS, 392, 630
Lenz P., Breger M., 2005, Commun. Asteroseismol., 146, 53
Lumb D. H., Schartel N., Jansen F. A., 2012, Opt. Eng., 51, 1009
Patterson J., 1979, ApJ, 231, 789
Politano M., Starrfield S., Truran J. W., Weiss A., Sparks W. M., 1995, ApJ, 448, 807
Ramsay G., Cropper M., 2003, MNRAS, 338, 219
Ramsay G., Cropper M., Wu K., Potter S., 1996, MNRAS, 282, 726
Schmidt G. D., Stockman H. S., 1991, ApJ, 371, 749
Schmidt G. D., Liebert J., Stockman H. S., 1995, ApJ, 441, 414
Schwope A. D. et al., 1998, in Howell S., Kuulkers E., Woodward C., eds, ASP Conf. Ser. Vol. 137, Wild Stars in the Old West. Astron. Soc. Pac., San Francisco, p. 44

Semeniuk I., Kruszewski A., Schwarzenberg-Czerny A., Chlebowski T., Mikolajewski M., Wolcyzk J., 1977, Acta Astron., 27, 301
Semeniuk I., Olech A., Nalezyty M., 1995, Acta Astron, 45, 747
Slavin A. J., O'Brien T. J., Dunlop J. S., 1995, MNRAS, 276, 353
Stockman H. S., Schmidt G. D., Lamb D. Q., 1988, ApJ, 332, 282
Warner B., 1995, Cataclysmic Variable Stars. Cambridge Univ. Press, Cambridge
Wickramasinghe D. T., Bailey J. A., Meggitt S. M. A., Ferrario L., Hough J., Touhy I. R., 1991, MNRAS, 251, 28
Wolff M. T., Wood K. S., Imamura J. N., 1999, ApJ, 526, 435

This paper has been typeset from a TEX/LATEX file prepared by the author.